

Viscoelastic analysis of stress distribution in balanced and unbalanced adhesively bonded single-lap joints with functionally graded adherends under the Reddy model

Siavash Haddad Soleymani^{1,*}, Mohammad Shishesaz¹, Reza Mosalmani¹

¹Department of Mechanical Engineering, Shahid Chamran University of Ahvaz, Ahvaz, Iran

ARTICLE INFO

ABSTRACT

Article history:

Received: 26 May 2019

Accepted: 02 December 2019

Keywords:

Adhesively bonded single-lap joint

Viscoelastic adhesive

functionally graded adherend

semi-analytical method

finite element method

In this study, shear and peel stress distributions in the viscoelastic adhesive layer of a single-lap joint (SLJ) with functionally graded (FG) adherends are investigated. The study focuses on the effect of different adherend profiles and material composition on the time-dependent stress concentration/distribution in balanced and unbalanced SLJs. For this purpose, the Reddy model is applied to the FG adherends and a three-parameter solid viscoelastic model is used to simulate the adhesive layer behavior. Using the first-order shear deformation theory for the FG adherends, the governing differential equations are derived and then transformed into the Laplace domain. A finite element model of the joint was also developed to further backup the numerical solution. The numerical inverse Laplace transform method was used to extract the desired results that were then compared with those of finite element method (FEM) findings. Very good agreements were observed between the results of both methods. Results show that the geometric and mechanical properties of the FG adherends have an essential role in reducing the shear and peel stress concentrations as well as the uniformity of shear stress distribution in the overlap region. Results also show that either method (finite element or the proposed semi-analytical method) can be utilized with confidence for prediction of stress relaxation in the adhesively bonded SLJs with FG adherends.

1. Introduction

Using adhesively bonded joints in structures and machines that are critical in terms of strength seems to be promising due to economic issues, ease, and speed of installation. Hence, it is important to determine the stress distribution in such joints. On the other hand, industrial adhesives are mainly made of polymeric materials that have viscoelastic properties. These properties should be considered while designing adhesively bonded joints. For this reason, stress distribution in the adhesively bonded single-lap joints (SLJs) has been widely investigated by many investigators [1-6]. The analysis of adhesively SLJs was first started by Volkersen [7] and developed by Goland and Reissner [8], followed by Hart-Smith [9]. In several studies, Luo and Tong [10-12] applied the higher-order displacement theories, as well as the large deflection of the adhesive layer, to investigate the stress distribution in single lap joints based on analytical solutions. The nonlinear analysis of SLJs of composite plates was covered as well. The theoretical model developed by Zhao *et al.* [13] was used to investigate the stress distribution in an unbalanced adhesively bonded SLJ. They used two-dimensional (2D) elasticity theory to perform their analysis in which they applied the complete strain-displacement and stress-strain relationships

for the adhesive and adherends, simultaneously. Selahi *et al.* [14] used two new techniques to calculate the stress distribution in composite SLJs; one on the basis of energy method and the other, based on the state-space equations. Liu and Huang [15] conducted the 2D analysis to determine the adhesive stresses in three kinds of adhesively bonded joints with mixed forced loadings and/or displacement boundary conditions. On the basis of the variational theorem, Zhao *et al.* [16] used a 2D analytical method to investigate the elastic stresses in symmetrically adhesively bonded SLJs, taking into account the longitudinal normal stress which varied linearly along the joint thickness. In two studies, Shishesaz and Reza [17, 18] investigated the stress distribution in a SLJ with composite adherends (single and multilayers) in presence of a crack in the overlap region.

To study the unbalanced SLJ stresses and edge moment factors, Jiang *et al.* [19] proposed an improved one-dimensional beam model considering the effects of interfacial compliance as well as the large deflections of the adherends and overlap. In another study, Jiang *et al.* [20] introduced a 2D stress distribution model on the quasi-static behavior of unbalanced fiber reinforced plastic (FRP) composite SLJs, taking into account the effects of large deformation, bending-tension coupling, and interfacial compliance. Assuming a nonlinear behavior for the adhesive, Selahi and Kadivar [21], presented a novel formulation, in

* Corresponding Author. Tel.: +98 9166439776; Fax: +98 42426666
Email Address: haddadsoleymani@gmail.com

conjunction with a numerical solution, to study the effects of edge loads on stress distribution in an adhesively bonded SLJ, with symmetric and asymmetric multilayer composite adherends. Talmon l'Armée *et al.* [22] introduced a new method for determination of bending moments and shear forces in SLJs with composite adherends that allowed the analysis of joints with asymmetrically laminated adherends exhibiting bending-extensional coupling. Their model was applicable to various types of boundary conditions (simply supported ends, fixed ends, strap repair, and bonded doubler).

The work of Delale and Erdogan [23] may be introduced as one of the first studies focusing on the viscoelastic analysis of adhesively SLJs. They analyzed an adhesively bonded lap joint based on three different external loads while assuming the isotropic adherends are elastic and the adhesive behaves as a linear viscoelastic material. Using a three-parameter viscoelastic solid model, they obtained the shear and peel stress distributions within the adhesive layer. Pandey *et al.* [24] performed a nonlinear finite element analysis on adhesively bonded joints considering the elasto-viscoplastic behavior for the adhesive material while taking into account joint the finite rotation. Nagaraja and Alwar [25] investigated the stress distribution in a viscoelastic adhesively bonded plane lap joint using the finite element method (FEM). Moreover, the viscoelastic analysis algorithm for bonded connections, based on finite element method (FEM), was presented by Yadagiri *et al.* [26] as well as Carpenter [27]. Utilizing FEM, Groth [28] investigated the stress distribution in SLJs both with and without a crack, considering separate viscoelastic and viscoplastic behaviors for the adhesive layer. However, Sato [29], analytically solved for the residual stresses in the adhesive layer, encapsulated by two adherends with different curvatures, while assuming the adherends behave as linear elastic beams and the adhesive layer behaving as linear viscoelastic springs. Shishesaz and Reza [30], studied the effect of viscoelasticity of the adhesive layer on the shear stress distribution in an adhesively bonded SLJ with isotropic adherends under a tensile load. In another study, they [31] investigated the effect of a break in the laminated composite adherends on stress distribution in the adhesive layer, assuming a viscoelastic behavior for the adhesive and matrix. They concluded that viscoelastic behavior decreases the peak stress near the break. They also examined the effect of size and location of the break, as well as the effect of volume fraction of fibers, on stress distribution in the adhesive layer. Reza *et al.* [32] studied the effect of viscoelasticity of epoxy adhesive, on the creep behavior of the adhesive layer, in a double-lap joint. Moreover, the viscoelastic effect of the matrix used in polymeric composites on transient stress concentration in the intact fibers and the joint, due to a sudden break in the fibers, was the main issue in [33]. Here, the authors (Reza and Shishesaz) showed that assuming a viscoelastic behavior for the matrix decreases the peak stress concentration.

Recently, many studies have been conducted in the field of functionally graded (FG) adhesively bonded SLJs. It has been shown that varying Young's modulus of the adhesive along the overlap region results in more uniform stress distribution in the adhesive layer, and hence, reduces the stress concentration [34-37]. Apalak and Gonz [38, 39] investigated the 3D elastic stress state of adhesively bonded SLJs with FG adherends under the tensile and flexural loads. They used a layered shell finite element, based on classical laminated and higher-order theories, to analyze the stress distribution in composite plates. They concluded that the number of layers and the compositional gradient exponent of the FG adherends highly affect the through-thickness profiles and the

magnitudes of critical stress components in the adherends, as well as the adhesive layer. Guin and Wang [40] analyzed the stress distribution in adhesively bonded SLJs with FG adherends, using the three-parametric elastic foundation model for the adhesive layer. Amidi and Wang [41] introduced a viscoelastic analytical model for the adhesively bonded SLJs with FG adherends, in which the adhesive layer was modeled as a three-parameter viscoelastic foundation using a standard linear solid model. They showed that the FG adherend configuration and the mechanical properties of the adhesive layers play important roles in the uniformity of shear stress distribution along the overlap length. A theoretical framework for stress analysis of longitudinally material-tailored adhesively SLJs subjected to tensile load was presented by Khan *et al.* [42]. They developed a 2D elastic sandwich model for an unbalanced SLJ with compliance-tailored adherends and adhesive, allowing a power-law variation in the modulus along the longitudinal direction. They showed that in joints with subcritical and critical bond lengths, the material-tailoring of the adherends/adhesive reduces the peak stresses in the adhesive layer.

Considering the searched literature works, the present study concentrates on the adhesive shear and peel stress relaxation in an adhesively bonded SLJ with FG adherends under a tensile load. In the previous related studies ([40, 41]), only one profile for the through-thickness material composition of a balanced joint with the FG adherends was selected. This research aims to study the effect of different profiles for the FG adherend on the adhesive time-dependent stress distribution in the balanced and unbalanced SLJs. For this purpose, the Reddy model with the capability of changing the composition profile of functionally graded materials (FGMs) is used. The standard linear solid model (Zener model) is used to simulate the viscoelastic behavior of the adhesive layer. The finite element method is used to verify the analytical results. The solution which is obtained based on the application of a rather simple semi-analytical method allows for the comprehensive stress analysis in the joint while taking into account the effect of different parameters, especially the change in the material composition of the adherends. This method can lead to the correct selection of the components in a balanced and/or unbalanced adhesively bonded SLJ.

2. Initial assumptions and derivation of equations

2.1. Initial assumptions

The proposed 2D model of the SLJ considered in this work is consisted of two adherends joined by a thin layer of adhesive layer, uniform in thickness, as shown in Fig. 1. Additionally, the adherends are made of FG materials that are graded through their thicknesses and experience a tensile load T . It is assumed that they behave as linear elastic materials and encapsulate a thin linear viscoelastic adhesive layer. The variations in stresses along the adhesive thickness are ignored while the effects of axial and bending moment in the adhesive layer are neglected, due to its weak elastic modulus compared with those of the adherends. The x and z axes start from the middle of the adhesive layer, perpendicular to the joint edges, and in line with the joint loading. The adherend thicknesses are considered to be t_1 (top adherend, or adherend 1) and t_2 (bottom adherend, or adherend 2), respectively. The adhesive layer thickness, as well as the length of overlap region (joint), are assumed to be t_a and $2l$, respectively (see Fig. 1).

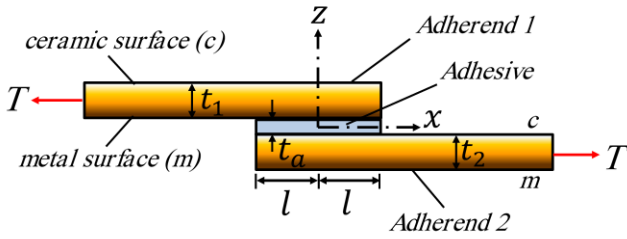


Figure 1. 2D view of an unbalanced single-lap joint with FG adherends.

The lower surfaces of both adherends are assumed to be made of metal while the upper surfaces are taken to be of pure ceramic. Furthermore, the material properties of both adherends are allowed to vary smoothly and continuously from metal to ceramic in the thickness direction. For the balanced joint, two different arrangements are postulated as follow (see Fig. 2):

Arrangement I: A balanced joint with the metal surfaces touching the adhesive layer.

Arrangement II: A balanced joint with the ceramic surfaces touching the adhesive layer.

The purpose of these arrangements is to attain the best configuration for tailoring the stress distribution in the joint and to achieve the optimal joint configuration with greater load capacity. Moreover, the use of the adhesive layer is to give additional insights to the pervious works in which the viscoelastic behavior of the adhesive layer and other parameters have been neglected.

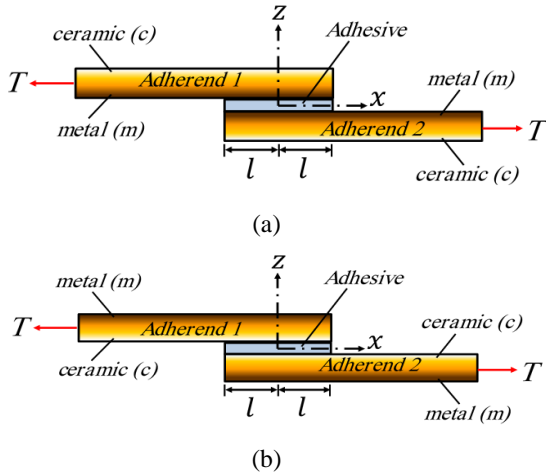


Figure 2. Two arrangement types for a balanced single-lap joint with FG adherends: (a) Arrangement I, (b) Arrangement II.

2.2. Derivation of equations

The Reddy model is adopted to derive the basic equations. Based on this model, the ceramic volume fraction V_c and the metal volume fraction V_m of the i^{th} adherend change in the thickness direction (i.e. z_i), measured from the mid-plane of the i^{th} adherend, according to the following equations.

$$V_c(z_i) = \left(\frac{1}{2} + \frac{z_i}{t_i}\right)^n, \quad V_m(z_i) = 1 - V_c(z_i) \quad i = 1, 2 \quad (1)$$

In this equation, n (as the volume fraction exponent) dictates the material variation profile through the thickness. Subscripts 1 and 2 correspond to the adherends 1 and 2, respectively. As n approaches zero, each adherend tends to behave as of pure ceramic. On the contrary, for n approaching infinity, each adherend behaves as a pure metal.

Furthermore, Young’s moduli of the adherends along their thicknesses are expressed as follows:

$$E_i(z_i) = \left(\frac{1}{2} + \frac{z_i}{t_i}\right)^n (E_c - E_m) + E_m \quad i = 1, 2 \quad (2)$$

Here, E_c and E_m are the elasticity moduli of the ceramic and metal respectively, with E_i being the elasticity modulus of the i^{th} adherend. Moreover, the changes in Poisson’s ratios across the thicknesses of both adherends are neglected due to the small changes in their magnitude.

It is necessary to mention that for better presentation of the deduced results and showing the effect of n on the joint behavior, instead of using n as a variable in the relevant figures/discussions (i. e. Fig. 14), parameter V_{ct} and V_{mt} , defined in Eq. (3) are used to show the exact values of ceramic and metal volume fractions (in each adherend) for any specific value of n . These parameters are obtained by integrating Eqs. (1) along the thickness, while using V_{ct} and V_{mt} for the volume fraction of the ceramic and metal phases, respectively.

$$V_{ct} = \frac{100}{n+1}, \quad V_{mt} = 1 - V_{ct} \quad i = 1, 2 \quad (3)$$

In accordance with the first-order shear deformation theory, longitudinal and transverse displacement for both adherends are expressed as:

$$U_i = u_i + z_i \varphi_i \quad i = 1, 2 \quad (4)$$

$$W_i = w_i$$

where, U_i and W_i are the axial and transverse displacements of a point in the i^{th} adherend and are functions of x , z , and time t . Additionally, u_i and w_i are the axial and transverse displacements of the mid-plane and φ_i is the cross-sectional rotation of the i^{th} adherend (see Fig. 3). These parameters are functions of x and t .

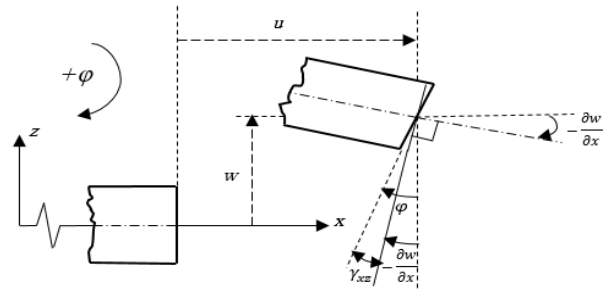


Figure 3. Undeformed and deformed geometries of the adherend edge under the assumption of first-order shear deformation theory.

Using the above first-order shear deformation equations for the FG adherends, we now try to derive the governing differential equations in the adhesive layer, which will then be transferred into the Laplace domain. On solving these equations and using the proper boundary conditions, the shear and peel stress distributions will be obtained in the adhesive layer. The desired results will be extracted in the time domain using a numerical inverse Laplace transform method. For this purpose, the strain-displacement equations for the two adherends are written as:

$$\epsilon_{ix} = \frac{\partial u_i}{\partial x} + z_i \frac{\partial \varphi_i}{\partial x} \quad i = 1, 2 \quad (5)$$

$$\gamma_{ixz} = \varphi_i + \frac{\partial w_i}{\partial x}$$

where, ϵ_{ix} and γ_{ixz} are the axial and shear strains related to the i^{th} adherend. Moreover, the axial force (N_i), transverse shear force (Q_i), and the bending moment (M_i) for each adherend are expressed as:

$$N_i = A_{11}^{(i)} \frac{\partial u_i}{\partial x} + B_{11}^{(i)} \frac{\partial \varphi_i}{\partial x} \quad i = 1, 2 \quad (6)$$

$$M_i = B_{11}^{(i)} \frac{\partial u_i}{\partial x} + D_{11}^{(i)} \frac{\partial \varphi_i}{\partial x}$$

$$Q_i = k_s A_{55}^{(i)} \left(\varphi_i + \frac{\partial w_i}{\partial x} \right) \quad i = 1, 2 \quad (7)$$

In Eq. (7), k_s is the shear correction factor (coefficient) which is used in the first-order shear deformation theory and is equal to 5/6. Additionally, $A_{11}^{(i)}, B_{11}^{(i)}$ and $D_{11}^{(i)}$ represent the extensional, coupling, and bending stiffness matrix elements for the i^{th} adherend and are obtained as follow:

$$[A_{11}^{(i)}, B_{11}^{(i)}, D_{11}^{(i)}] = \frac{1}{1 - \nu_i^2} \int_{-t_i/2}^{t_i/2} E_i(z_i) [1, z_i, z_i^2] dz_i \quad i = 1, 2 \quad (8)$$

$$A_{55}^{(i)} = \frac{1}{2(1 + \nu_i)} \int_{-t_i/2}^{t_i/2} E_i(z_i) dz_i = \frac{1 - \nu_i}{2} A_{11}^{(i)} \quad i = 1, 2 \quad (9)$$

where ν_i is the Poisson's ratio of the i^{th} adherend. Consequently, Eqs. (6) and (7) are recast as:

$$\begin{cases} \frac{\partial u_i}{\partial x} = a_i N_i + b_i M_i \\ \frac{\partial \varphi_i}{\partial x} = b_i N_i + d_i M_i \\ \frac{\partial w_i}{\partial x} = c_i Q_i - \varphi_i \end{cases} \quad i = 1, 2 \quad (10)$$

The coefficients of $a_i, b_i, c_i,$ and d_i are given in Appendix A.

Figure 4 shows the Free-body diagram of an infinitesimal element of the joint with length dx . In this figure, τ and σ are the shear and peel stresses in the adhesive layer, respectively. Compared to the adherends, the adhesive thickness is small and hence the changes in these two stress components along the adhesive thickness are ignored. In other words, the two stress components are assumed to be only functions of x and t . Furthermore, as mentioned before, due to a weak elastic modulus of the adhesive layer (compared to the adherend), the longitudinal and transverse loads in this component are discarded. Moreover, the resultant loads on each individual adherend and adhesive layer are selected at their mid-layers, since this notation is customary in all drawings used in the literature (i. e. Ref. [43] and many others dealing with FG adherends) and appears to produce accurate results.

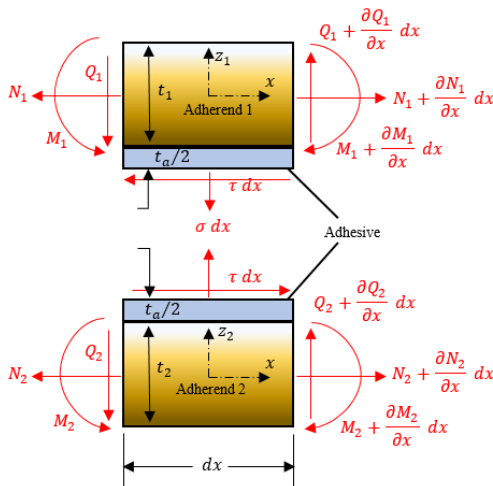


Figure 4. Free-body diagram of an infinitesimal element in the overlap region.

Now, to derive the equilibrium equations, referring to Fig. 4, based on the forces and moments equilibrium for each adherend (and a portion of its neighboring adhesive layer), and considering $h_1 = \frac{t_1}{2}, h_2 = \frac{t_2}{2}$ and $h_a = \frac{t_a}{2}$, it is concluded that:

$$\begin{aligned} \frac{\partial N_1}{\partial x} = \tau & , \quad \frac{\partial N_2}{\partial x} = -\tau \\ \frac{\partial Q_1}{\partial x} = \sigma & , \quad \frac{\partial Q_2}{\partial x} = -\sigma \\ \frac{\partial M_1}{\partial x} = Q_1 - \tau(h_1 + h_a) & , \quad \frac{\partial M_2}{\partial x} = Q_2 - \tau(h_2 + h_a) \end{aligned} \quad (11)$$

The longitudinal normal strain ϵ_x , the transverse normal strain ϵ_z , and the shear strain γ_{xz} in the adhesive layer can be written in terms of the displacements and rotations as:

$$\epsilon_x = \frac{1}{2} \left(\frac{\partial u_1}{\partial x} - h_1 \frac{\partial \varphi_1}{\partial x} + \frac{\partial u_2}{\partial x} + h_2 \frac{\partial \varphi_2}{\partial x} \right) \quad (12)$$

$$\epsilon_z = \frac{1}{t_a} (w_1 - w_2) \quad (13)$$

$$\gamma_{xz} = \frac{1}{t_a} (u_1 - h_1 \varphi_1 - u_2 - h_2 \varphi_2) \quad (14)$$

Assuming a viscoelastic behavior for the adhesive layer, based on the three-parameter solid model (the Zener model), the stress-strain relationships for adhesive layer in Laplace domain are written as follows:

$$\bar{\sigma} = \bar{A}_1 \bar{\epsilon}_z + \bar{A}_2 \bar{\epsilon}_x \quad (15)$$

$$\bar{\tau} = \bar{A}_3 \bar{\gamma}_{xz} \quad (16)$$

where ‘ $\bar{\quad}$ ’, represents any specific parameter in the Laplace domain. The coefficients $\bar{A}_1, \bar{A}_2,$ and \bar{A}_3 are given in Appendix B. Performing math operations on Eqs. (15) and (16) which are given in Appendix C, the two governing differential equations for stresses in the adhesive layer (in the Laplace domain) are obtained as:

$$\left\{ \begin{aligned} \frac{\partial^4 \bar{\sigma}}{\partial x^4} + \alpha_1 \frac{\partial^3 \bar{\tau}}{\partial x^3} + \alpha_2 \frac{\partial^2 \bar{\sigma}}{\partial x^2} + \alpha_3 \frac{\partial \bar{\tau}}{\partial x} + \alpha_4 \bar{\sigma} &= 0 \\ \frac{\partial^3 \bar{\tau}}{\partial x^3} + \beta_1 \frac{\partial \bar{\tau}}{\partial x} + \beta_2 \bar{\sigma} &= 0 \end{aligned} \right. \quad (17)$$

$$\left\{ \begin{aligned} \frac{\partial^4 \bar{\sigma}}{\partial x^4} + \alpha_1 \frac{\partial^3 \bar{\tau}}{\partial x^3} + \alpha_2 \frac{\partial^2 \bar{\sigma}}{\partial x^2} + \alpha_3 \frac{\partial \bar{\tau}}{\partial x} + \alpha_4 \bar{\sigma} &= 0 \\ \frac{\partial^3 \bar{\tau}}{\partial x^3} + \beta_1 \frac{\partial \bar{\tau}}{\partial x} + \beta_2 \bar{\sigma} &= 0 \end{aligned} \right. \quad (18)$$

The coefficients $\alpha_i (i = 1, \dots, 4)$ and $\beta_i (i = 1, 2)$ are given in terms of other parameters in Appendix C. For the unbalanced joint, all coefficients α_i and β_i are nonzero. On solving Eq. (18) for $\bar{\sigma}$ and substituting the result back into Eq. (17), the seventh-order linear differential equation for the shear stress is obtained as:

$$\frac{\partial^7 \bar{\tau}}{\partial x^7} + \gamma_1 \frac{\partial^5 \bar{\tau}}{\partial x^5} + \gamma_2 \frac{\partial^3 \bar{\tau}}{\partial x^3} + \gamma_3 \frac{\partial \bar{\tau}}{\partial x} = 0 \quad (19)$$

where the coefficients $\gamma_i (i = 1, \dots, 3)$ are expressed in Eq. (20);

$$\begin{aligned} \gamma_1 &= \alpha_1 + \beta_1 \\ \gamma_2 &= \alpha_2 + \alpha_1 \beta_1 - \alpha_3 \beta_2 \\ \gamma_3 &= \alpha_2 \beta_1 - \alpha_4 \beta_2 \end{aligned} \quad (20)$$

On solving Eq. (19), the adhesive shear stress distribution in the Laplace domain is expressed as:

$$\bar{\tau} = \sum_{i=1}^3 [F_i \sin h \lambda_i x + H_i \cos h \lambda_i x] + C \quad (21)$$

Equation (21) is the general solution to Eq. (19) and it can be found in any related math book. Also, substituting Eq. (21) into Eq. (18) and solving for $\bar{\sigma}$, the peel stress distribution in the adhesive layer (in the Laplace domain) is expressed as:

$$\bar{\sigma} = -\frac{1}{\beta_2} \sum_{i=1}^3 \{\lambda_i(\lambda_i^2 + \beta_1)[F_i \cos h \lambda_i x + H_i \sin h \lambda_i x]\} \quad (22)$$

Equation (22) is simply obtained by substituting Eq. (21) into (18) and simplifying the result. In Eqs. (21) and (22), $F_i (i = 1, \dots, 3)$, $H_i (i = 1, \dots, 3)$, and C are the integration constants yet to be determined and are functions of 's' (Laplace variable). On application of boundary conditions defined in Appendix D, these constants are determined and substituted back in the shear and peel stress expressions given in the Laplace domain. In these equations, $\lambda_i (i = 1, \dots, 3)$ are defined as:

$$\lambda_1 = \sqrt{r_1} \quad , \quad \lambda_2 = \sqrt{r_2} \quad , \quad \lambda_3 = \sqrt{r_3} \quad (23)$$

where $r_i (i = 1, \dots, 3)$ are the roots of the following characteristic equation:

$$r^3 + \gamma_1 r^2 + \gamma_2 r + \gamma_3 = 0 \quad (24)$$

Taking the inverse Laplace transform of Eqs. (21) and (22) through a numerical scheme, the shear and peel stresses (as a function of time) in the overlap region are obtained using the MATLAB software program.

For a balanced joint, since $a_2 = a_1, b_2 = -b_1, c_2 = c_1$, and $d_2 = d_1$, then one can conclude that $\alpha_1 = \alpha_3 = \beta_2 = 0$. Therefore, equations for the peel and shear stresses in a balanced joint are recast as:

$$\left\{ \begin{aligned} \frac{\partial^4 \bar{\sigma}}{\partial x^4} + \alpha_2 \frac{\partial^2 \bar{\sigma}}{\partial x^2} + \alpha_4 \bar{\sigma} &= 0 \end{aligned} \right. \quad (25)$$

$$\left\{ \begin{aligned} \frac{\partial^3 \bar{\tau}}{\partial x^3} + \beta_1 \frac{\partial \bar{\tau}}{\partial x} &= 0 \end{aligned} \right. \quad (26)$$

As observed, the two governing equations are now uncoupled and can be solved individually. Coefficients α_2, α_4 , and β_1 for the balanced joint are given in Appendix E. Considering the symmetry, distribution of shear and peel stresses in the adhesive layer for the balanced joint are expressed as:

$$\bar{\sigma} = R_1 \cos h \lambda_1 x + R_2 \cos h \lambda_2 x \quad (27)$$

$$\bar{\tau} = R_3 \cos h \lambda_3 x + R_4 \quad (28)$$

In these two equations, the unknown coefficients $R_i (i = 1, \dots, 4)$ are a function of 's' and can be determined on proper

application of boundary conditions. Moreover, in these two equations, $\lambda_i (i = 1, \dots, 3)$ are expressed by the following relations:

$$\lambda_1 = \sqrt{r_1} \quad , \quad \lambda_2 = \sqrt{r_2} \quad , \quad \lambda_3 = \sqrt{-\beta_1} \quad (29)$$

where $r_i (i = 1, 2)$ are the roots of the following characteristic equation:

$$r^2 + \alpha_2 r + \alpha_4 = 0 \quad (30)$$

Taking the inverse Laplace transform of Eqs. (27) and (28) through a numerical scheme, the shear and peel stresses (as a function of time) in the overlap region are obtained, using the MATLAB software program.

3. Numerical results and discussions

In this section, the numerical results are deduced for further discussion. Moreover, a 2D finite element analysis of the joint was performed to further verify the analytical results, using ANSYS v14 software program. The generated finite element model was based on the initial assumptions given before (see Fig. 5). The element used to mesh the model (both for the adhesive and adherends) was the 2D solid Quad 4 node 182 in the plane strain state. The mesh was refined near the overlap ends to obtain more accurate results at these locations (see Fig. 5). To model the functional behavior of the adherends, their thicknesses were divided evenly into eleven distinct homogenous isotropic layers with different mechanical properties. The material of each layer was selected based on the FG adherend properties. Also, to implement the viscoelastic properties of the adhesive layer, the Prony series option in the ANSYS software was invoked. The material and dimensional properties of the joint are given in Table 1. In this Table, E_a and ν_a are the elastic modulus and Poisson's ratio of the adhesive at time zero, respectively. Also, G_0 and G_∞ correspond to the adhesive shear moduli at times zero and infinity, respectively ($G_0 = E_a / 2(1 + \nu_a)$). The joint was assumed to be simply supported by a hinge located at the left end of the assembly while simply supported on the other end. The size of elements was changed up to a point where convergence in results was obtained.

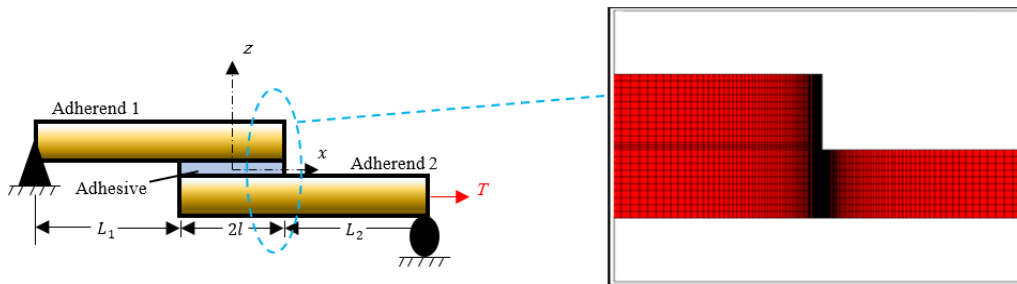


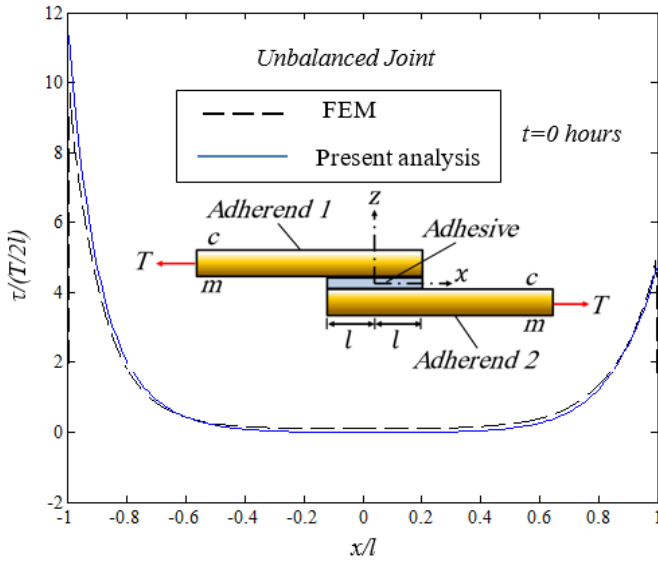
Figure 5. Assumed supporting conditions and meshing configuration of the finite element model.

Table 1. Joint geometry and mechanical properties of adhesive and adherends.

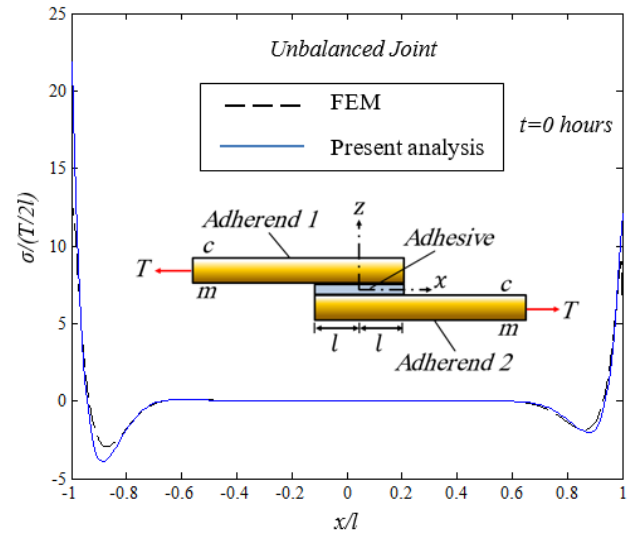
	Mechanical Properties		Thickness	Length
FG Adherend 1	$E_c = 380 \text{ GPa}$ $E_m = 70 \text{ GPa}$ $n=2$	$\nu_1 = 0.3$	$t_1 = 1 \text{ mm}$	$L_1 + 2l = 100 \text{ mm}$
FG Adherend 2	$E_c = 380 \text{ GPa}$ $E_m = 70 \text{ GPa}$ $n=2$	$\nu_2 = 0.3$	$t_2 = 1 \text{ mm}$	$L_2 + 2l = 100 \text{ mm}$
Viscoelastic Adhesive	$E_a = 3.2 \text{ GPa}$ $G_\infty = 0.2 G_0$ Relaxation time=5 hours	$\nu_a = 0.4$	$t_a = 0.1 \text{ mm}$	$2l = 20 \text{ mm}$

To investigating the time effect of viscoelastic properties of the adhesive layer on the shear and peel stress distributions in an unbalanced joint, the two stress components were plotted in Figs. 6(a), (b), (c), and (d). The deduced results in the first two figures are based on time $t = 0$, while the latter two (Figs. 6(c) and 6(d)) show the corresponding distributions after $t = 10$ hours. For further comparison and verification of the numerical results, the finite element findings are superimposed. Similar results for a balanced joint (Arrangement I) are shown in Fig. 7. Moreover, the finite element results are superimposed on Fig. 7

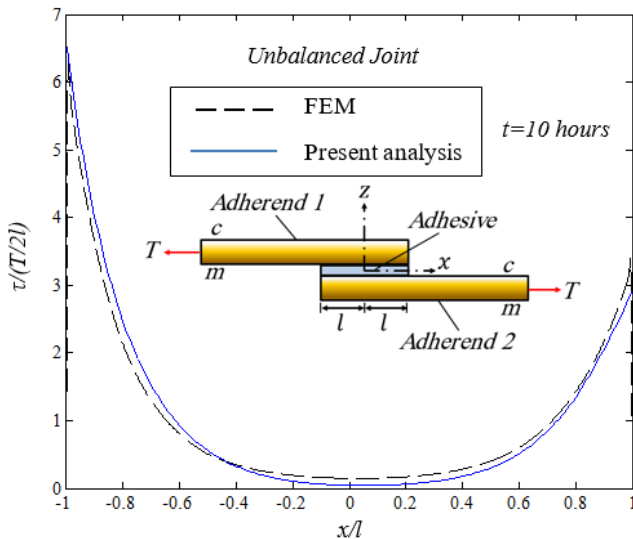
to further verify and backup the numerical results of the balanced model. These results are based on the analyses performed in the mid-surface of the adhesive layer. According to both figures, the unbalanced joint produces smaller peak shear and peeling stresses in the joint (adhesive layer). This effect is more prominent in the case of shear stresses. However, with any pass in time, the shear stress in the middle of the bond line increases, resulting in a more gradual change in its magnitude. Obviously, this effect cannot be predicted by any elastic analyses of such joints.



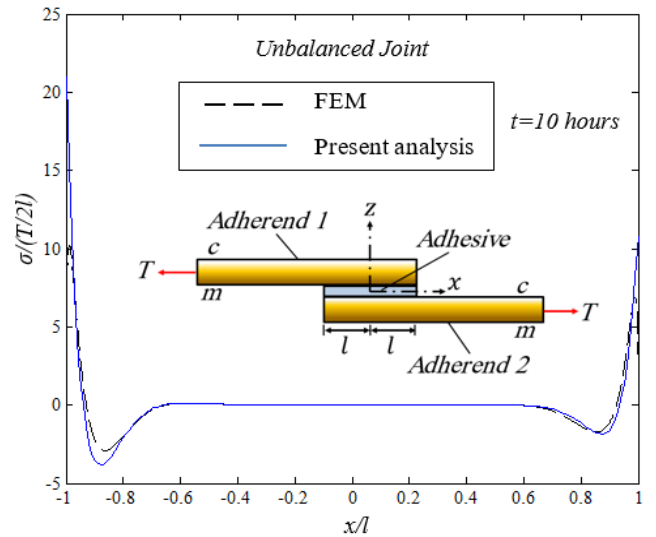
(a)



(b)



(c)



(d)

Figure 6. Comparison of the present semi-analytical method on the shear and peel stress distribution with those of FEM findings in an unbalanced SLJ with FG adherends under tensile load of $T = 100$ N at $t = 0$ ((a) and (b)), and $t = 10$ hours ((c) and (d)).

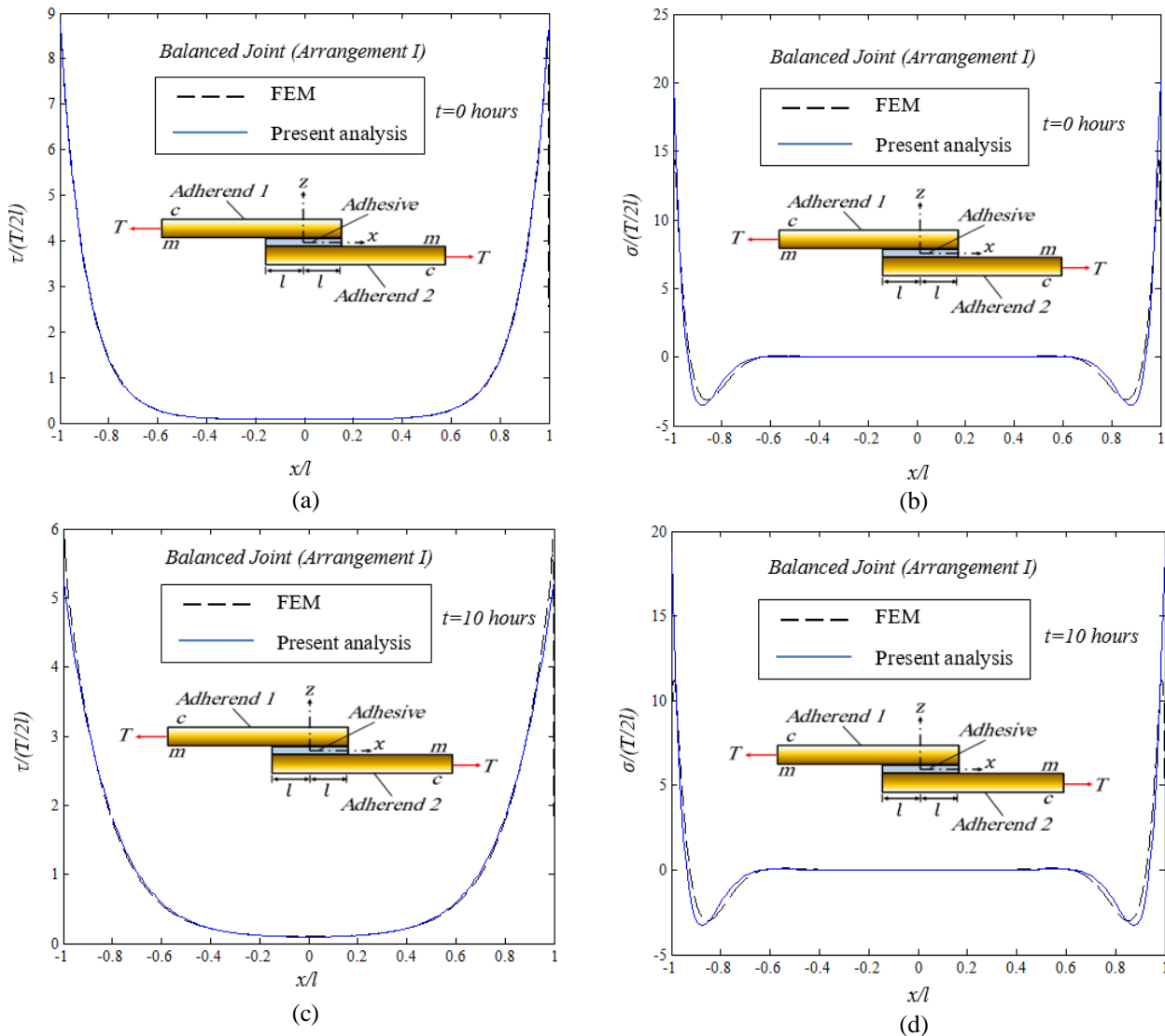


Figure 7. Comparison of the present semi-analytical method on the shear and peel stress distribution with those of FEM findings in a balanced SLJ (Arrangement I) with FG adherends under tensile load of $T = 100$ N at $t = 0$ ((a) and (b)), and $t = 10$ hours ((c) and (d)).

In the sequel, the effect of viscoelastic parameters and relaxation time on the distribution of stresses in the overlap region, forces, moments, and other parameters will be studied and discussed. For this purpose, the standard linear solid model parameters (η_1 , G_1 , and G_0) that are defined in Appendix B were used to simulate the behavior of postulated viscoelastic model in the adhesive layer. The results are shown in Figs. 8(a), 8(b), and 8(c), for different values of η_1 , G_1 , and G_0 . According to Fig. 8(a), as η_1 increases, the relaxation time increases while the peak values of shear stress remain intact at times zero and infinity. However, G_1 affects both the relaxation time and the corresponding values of shear stresses. As shown in Fig. 8(b), any rise in G_1 reduces the relaxation time while increasing the relaxed values of shear stresses without affecting their peak values at time zero. Moreover, according to Fig. 8(c), the effect of G_0 on the peak shear stresses is manifold. As G_0 increases, the initial and final states of the shear at times zero and infinity increase without a considerable effect on the relaxation time.

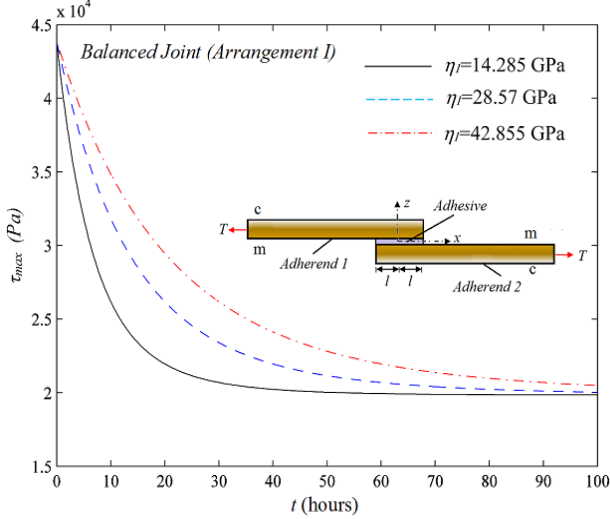
Figure 9 shows the changes in force and moment resultants (N , Q , and M) in the adherend 1 along the overlap region for three different time periods. As shown, the values of these parameters at the two ends of the overlap region exactly satisfy the boundary conditions. It is also observed that although the values of transverse shear Q_1 do not seem to be much dependent

on the time (for the time interval shown), the changes in normal load N_1 and the bending moment M_1 in adherend1 become more gradual, as the time passes from zero to fifty hours. Similar results are obtained in adherend 2 (results are not shown).

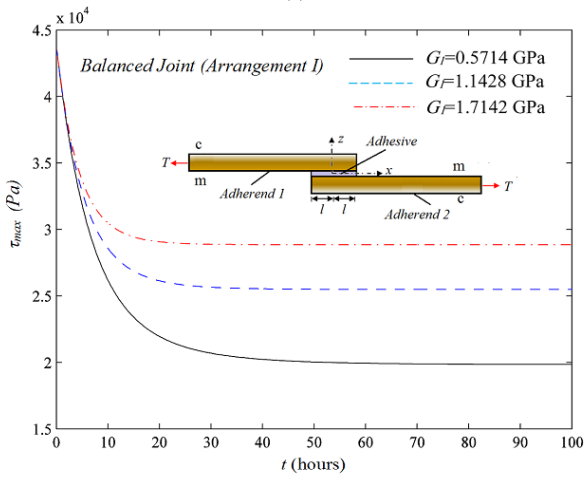
Through-thickness distributions of the transverse shear stress in adherend 1 at the beginning and mid-section of the overlap region are shown in Figs. 10(a) and 10(b) at $x = -l$ and $x = 0$, respectively. Three different time spans of $t = 0$, 10, and 50 hours were used. As shown in both figures, the zero shear stress boundary condition ($\tau_{xz} = 0$ at $z = 0.5$ mm) is met at the top free surface of adherend 1 ($t_1 = 1.0$ mm). This figure also indicates that the values of transverse shear stress (τ_{xz}) at the middle of the overlap region ($x = 0$) are much smaller than those appearing at the left end of the bond ($x = -l$) and are almost negligible compared to the others. With the pass of time, the maximum transverse shear stresses in the through-thickness direction of the adherend decrease and approach values closer to zero.

Figure 11 shows the through-thickness distribution of axial displacement u in the adherend 1 at the mid-section of the overlap ($x = 0$) for the three different time periods. As shown, the slope of adherend's edge (ϕ) (which is constant for all values of z at any location, i.e. $x = 0$) decreases while the axial displacement of the adherend midplane increases with time. The

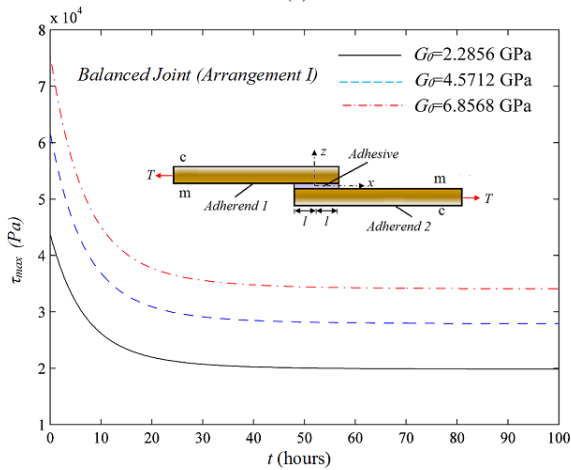
changes in both parameters do not seem to be much over a time period of 50 hours.



(a)

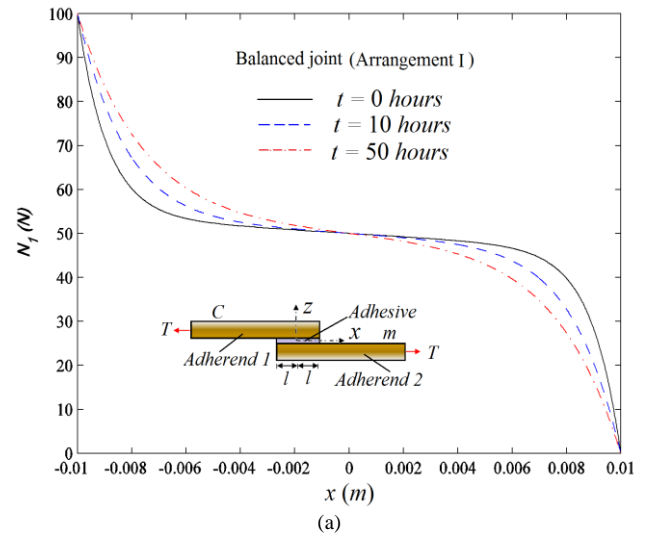


(b)

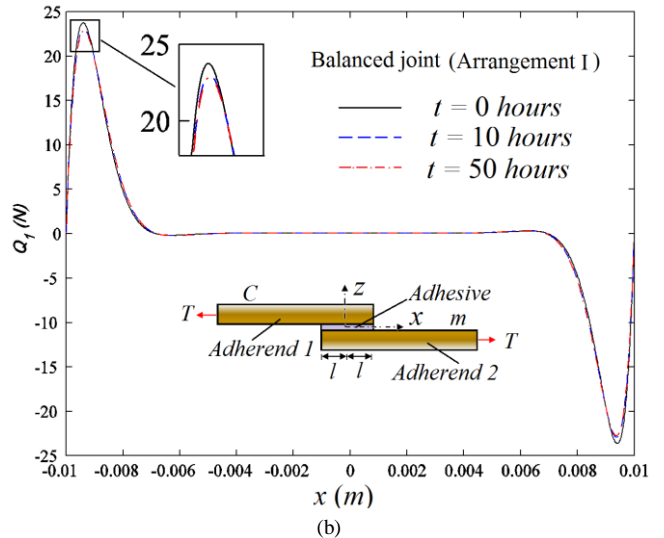


(c)

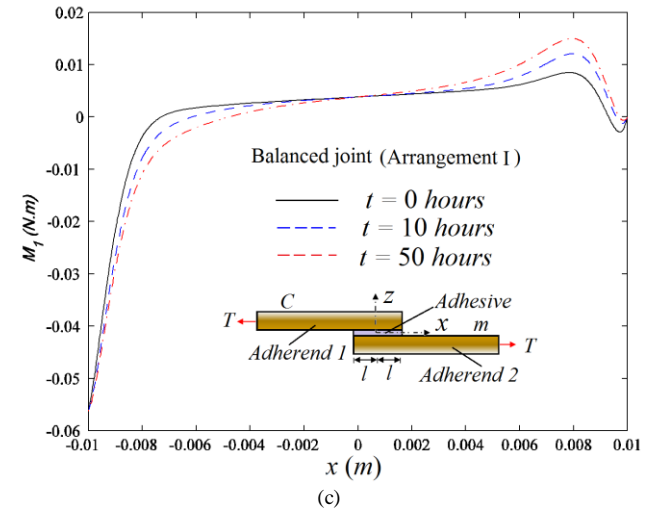
Figure 8. The effect of the standard linear solid model parameters on the maximum shear stress in adhesive layer of a balanced SLJ (Arrangement I) with FG adherends under a tensile load of $T = 100$ N. (a) η_I parameter, (b) G_I parameter, and (c) G_0 parameter.



(a)



(b)



(c)

Figure 9. Forces and moment distribution in FG adherends 1 along the overlap region of the balanced SLJ (Arrangement I) under a tensile load of $T = 100$ N at $t = 0, 10, 50$ hours: (a) axial force, (b) transverse force, and (c) bending moment.

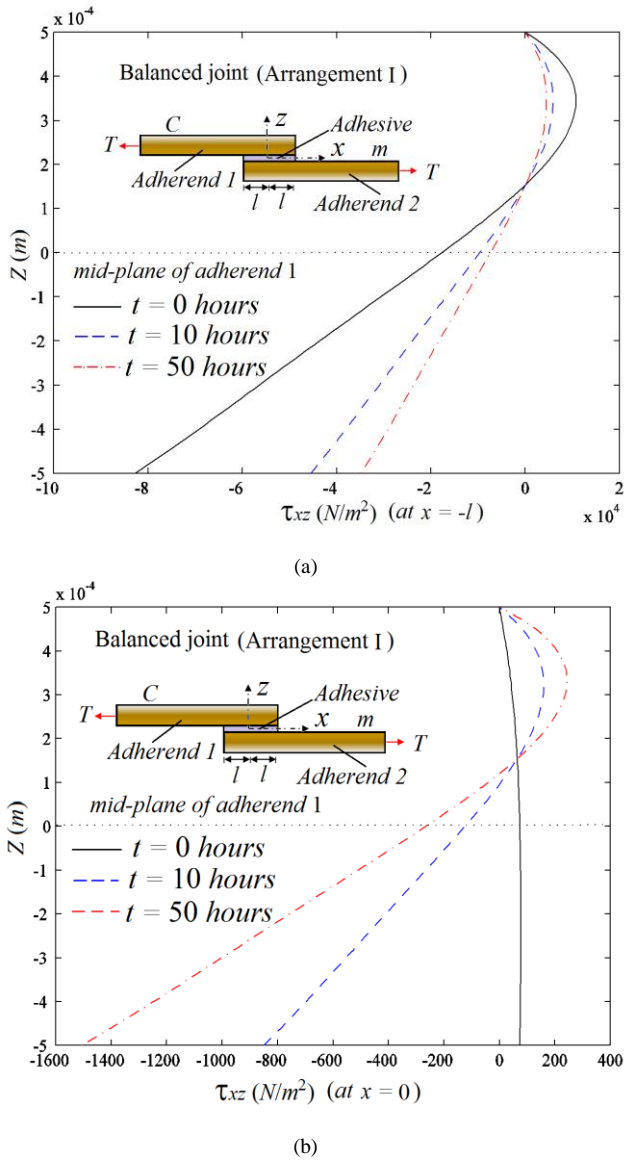


Figure 10. Through-thickness distribution of the transverse shear stress in the FG adherends 1 of the balanced SLJ (Arrangement I) under a tensile load of $T = 100$ N at $t = 0, 10, 50$ hours: (a) at the beginning of the overlap region, (b) at the middle of the overlap region.

Further influences of other mechanical and geometric parameters on the shear and peel stress distributions are discussed separately in the following sections. Additional analyses are performed on the balanced and unbalanced adhesively bonded SLJs with FG adherends to deduce these results. The material and geometric properties given in Table 1 are used throughout corresponding calculations; unless otherwise stated. Additionally, as mentioned before, instead of using ‘ n ’ as the volume fraction exponent, its equivalent

counterpart, namely the total volume fraction V_{ct} , is used for a better presentation of the results.

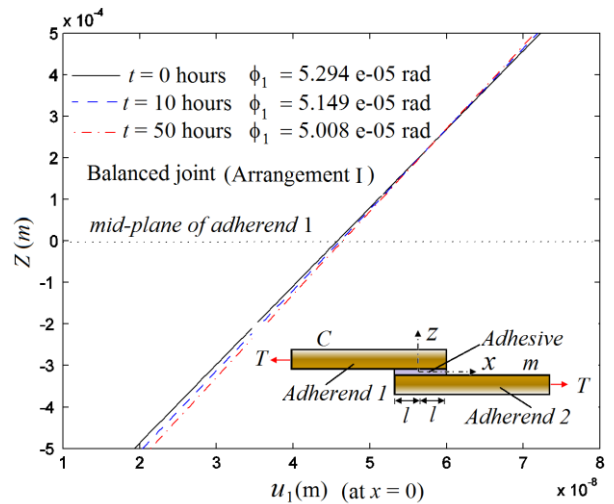


Figure 11. Transverse distribution of axial displacement and the rotation angle of section for FG adherends 1 in the middle of the overlap rejoin (at $x = 0$) in a balanced SLJ (Arrangement I) under a tensile load of $T = 100$ N at $t = 0, 10, 50$ hours.

3.1. Effect of volume fraction exponent n

In this section, the effect of material composition of the FG adherends on the adhesive stress distributions in the SLJ is investigated for three different time periods of $t = 0, 10, 50$ hours. For this purpose, three different ceramic-rich ($n = 0.1$), metal-rich ($n = 10$) and linear material composition ($n = 1$) are selected for the FG adherends. The results for the unbalanced (arrangement E) joints are presented in Figs. 12 and 13, respectively. It is observed that for any time period, reducing the value of parameter n (increasing the ceramic phase V_{ct} in the FG adherends) causes a significant reduction in the peak shear stresses developed in the adhesive layer (in both balanced and unbalanced joints). These stresses occur at the left end (unbalanced joint) or both ends (balanced joint) of the overlap region. Furthermore, the amount of shear stress in the middle of the joint increases slightly with any pass in time. Similar behavior is observed for the peel stress component except that the effects of time and n seem to be less prominent on this stress component. Moreover, as expected, the two stress components decrease at both ends of the overlap region while increasing in the mid-length, due to viscoelastic properties of the adhesive layer. This behavior is observed for all values of volume fraction exponent n . Moreover, results in Fig. 12 indicate that for any selected time period, the peak shear and peeling stresses that occur at the left end of the overlap region for an unbalanced joint are higher than those produced in a balanced joint (see Fig. 13) with similar geometric and mechanical properties of constituents.

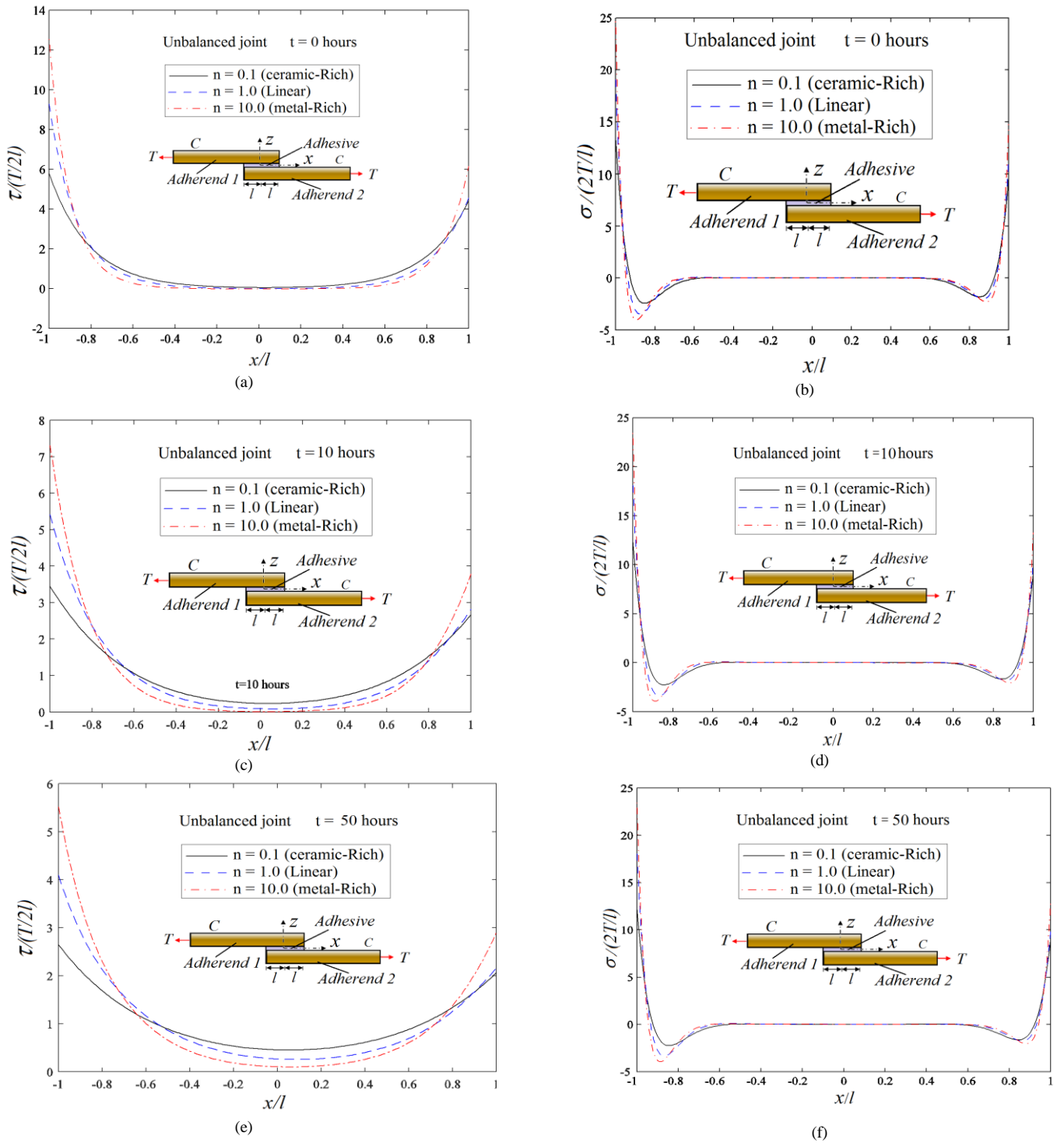


Figure 12. Normalized time-dependent adhesive shear and peel stress distributions for various Reddy model index in an unbalanced SLJ with FG adherends under a tensile load of $T = 100$ N at $t = 0$ ((a) and (b)), $t = 10$ ((c) and (d)), and $t = 50$ hours ((e) and (f)).

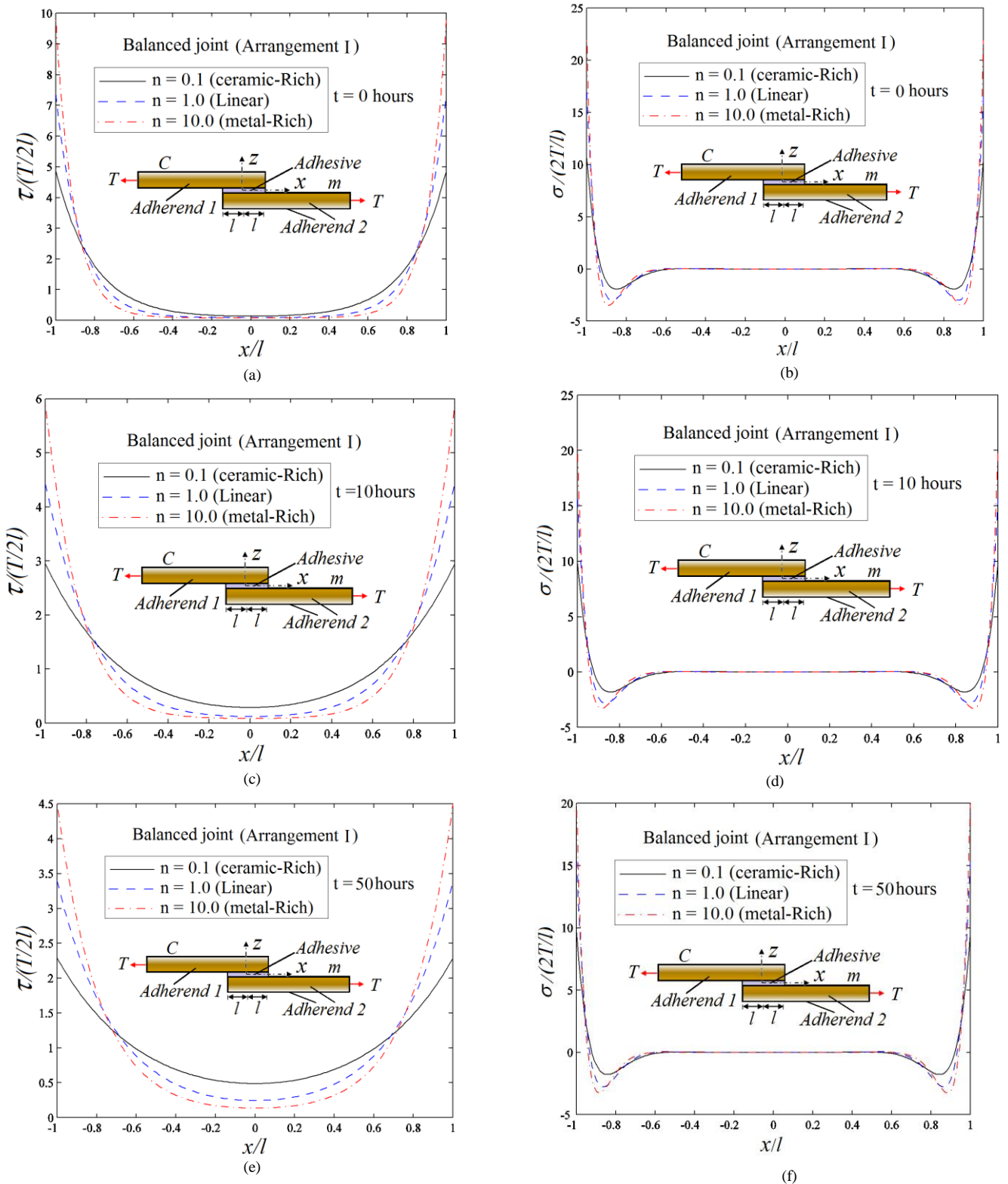


Figure 13. Normalized time-dependent adhesive stress distributions based on three different Reddy model indices in a balanced SLJ (Arrangement I) with FG adherends under a tensile load of $T = 100$ N at $t = 0$ ((a) and (b)), $t = 10$ ((c) and (d)), and $t = 50$ hours ((e) and (f)).

3.2. Effect of joint configuration

Previous studies have reported that stress concentration in the adhesive layer of a balanced joint with FG adherends is smaller when the stiffer material is placed nearest to the adhesive layer. This result has been achieved only for one profile of adherends material composition. In this section, the effect of FG adherends configurations on the adhesive stresses concentration is investigated for different adherends composition profiles. For

this purpose, the maximum shear and peel stresses are plotted versus V_a for the two arrangements of I and II, in a balanced adhesively SLJ, for the three different times periods mentioned before. Material properties and joint geometry are selected according to Table 1; except for n that is considered to be a variable.

As shown in Figs. 14a and 14b, although the maximum stresses in the two arrangements I and II are relaxed over time,

arrangement II always exhibits lower values of stresses compared with those in arrangement I, for $0 < V_{ct} < 100$. However, the differences in shear stresses for the two arrangements, at any time period, decrease with any increase in V_{ct} (lower values of n , corresponding to higher concentration of ceramic phase). Similar behavior is observed for the differences in peel stresses in both arrangements. The highest differences in the maximum shear and peel stresses (for the two arrangements) that occur at $V_{ct} \approx 25\%$ are equal to 34% and 43%, respectively. It is worth to mention that $V_{ct} = 0\%$ and $V_{ct} = 100\%$ correspond to the adherends with complete homogeneous metallic and ceramic properties, respectively. Additionally, according to the results in both figures, for arrangement I, the effect of ceramic phase volume fraction on reducing the maximum values of these stresses (see section 3.1 or Figs. 12 and 13) is higher for $V_{ct} > 25\%$.

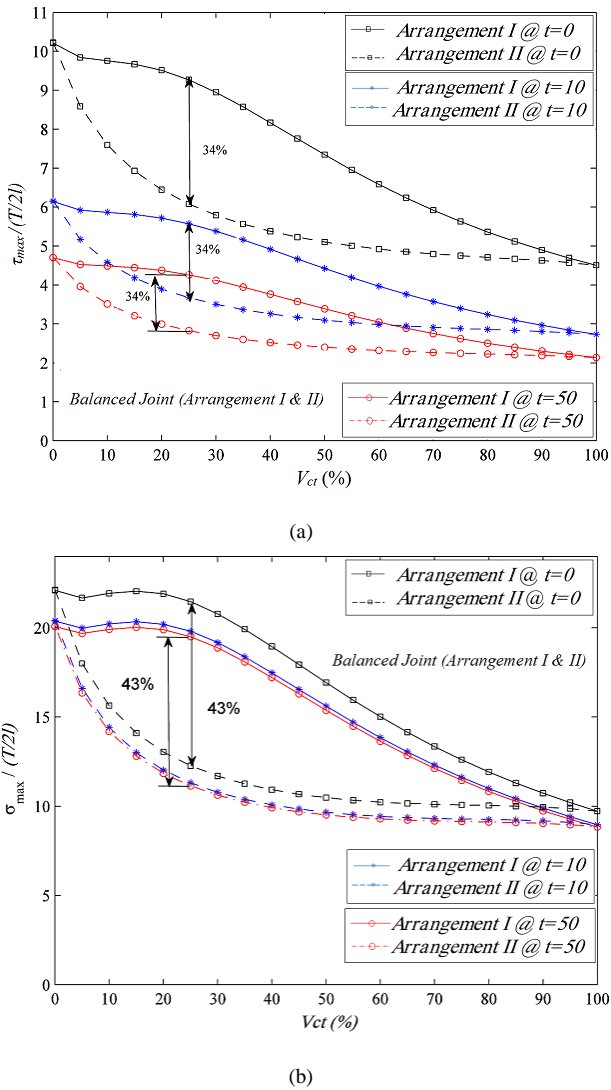


Figure 14. Comparison of maximum normalized adhesive peel and shear stresses in a balanced adhesively SLJ with FG adherends for arrangements I and II ($0 \leq V_{ct} \leq 100$), under a tensile load of $T = 100$ N for different time periods of $t = 0, 10$, and 50 hours: (a) shear stress, and (b) peel stress.

3.3. Effect of thickness and stiffness of the adhesive layer

In this section, the effects of thickness and stiffness (in elastic state or time zero) of the adhesive layer on the maximum values of shear and peel stresses in the viscoelastic adhesive layer are investigated. For this purpose, two FG adherends in a balanced state (arrangement I) and properties given in Table 1 are selected

to perform the analysis. In each run, a different composition for the FG adherends (ceramic-rich and metal-rich) was selected to seek the effects of adhesive thickness (in conjunction with the material composition of the adherend) on the two forgoing stress distributions (see Figs. 15(a) and 15 (b)). Two different values of $t_a = 0.1$ mm and 0.2 mm were selected for the adhesive thickness. Similar plots are also generated to investigate the effects of adhesive Young's modulus on the peel and shear stresses developed in the adhesive layer (see Figs. 16(a) and 16(b)).

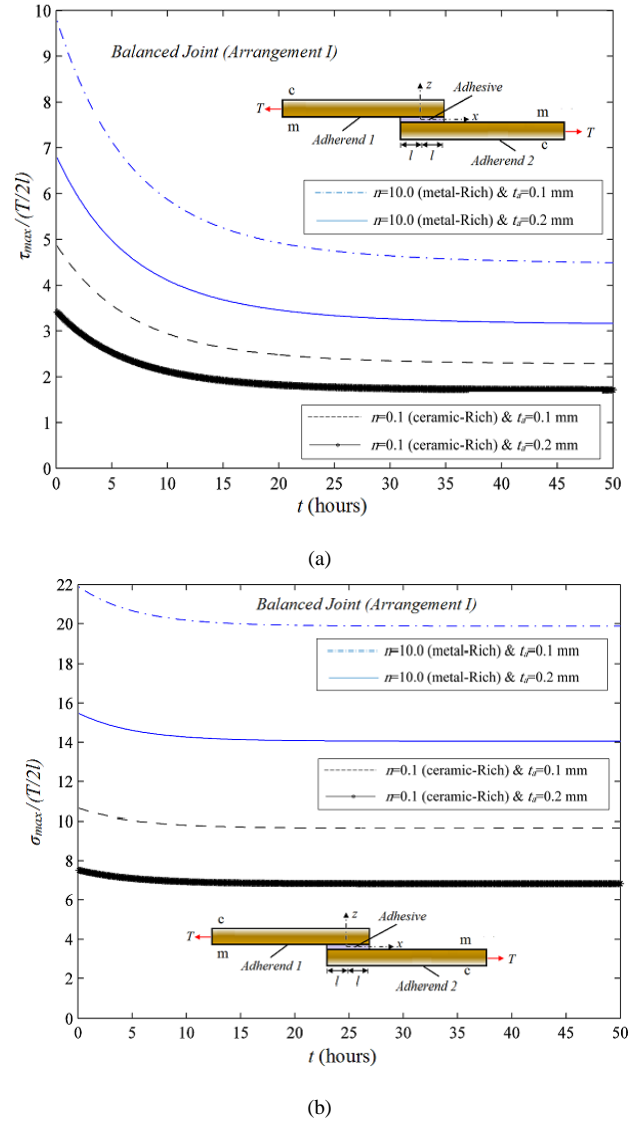


Figure 15. The effect of adhesive thickness on the maximum normalized shear and peel stresses in the adhesive layer during the time, for two different values of n in the balanced SLJ (Arrangement I) with FG adherends under tensile load: (a) shear stress and (b) peel stress.

As shown in these figures, stress concentrations in the joint are reduced by an increase in the adhesive thickness or a reduction in Young's modulus of the adhesive layer. This behavior is observed for both limiting values of FG adherends compositions (ceramic-rich with $n = 0.1$ and metal-rich with $n = 10$), with/without considering the adhesive viscoelastic behavior. It is also noticed that the stress relaxation value for the peel stress (about 9%) is much smaller than that of the shear stress (about 55%). Additionally, according to both figures, the stress stabilization time for peeling stress is about 21 hours and that for the shear stress is about 36 hours.

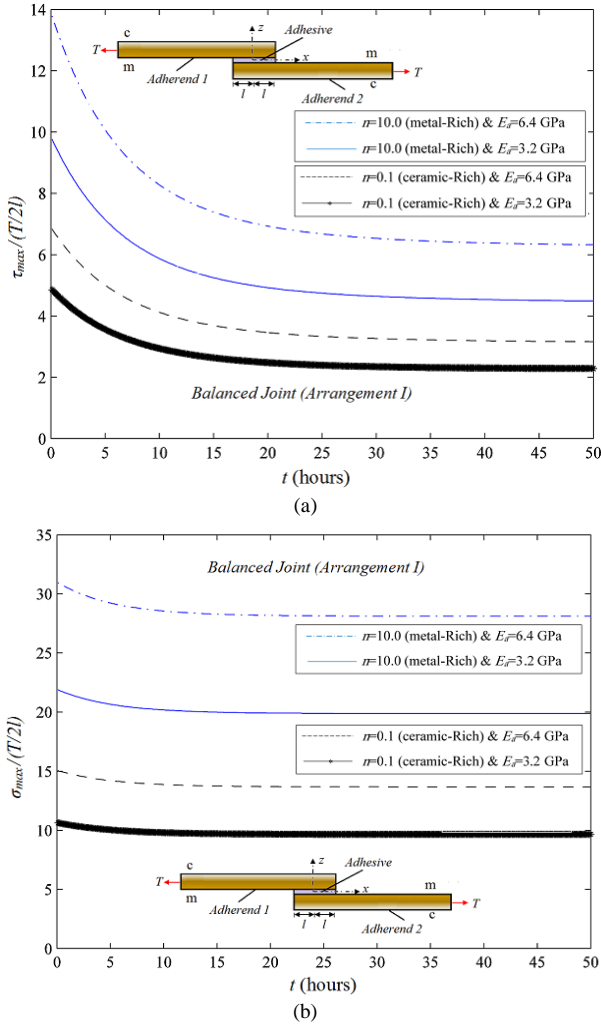


Figure 16. Impact of adhesive stiffness on the maximum normalized stresses in the adhesive layer during the time, for the two different values of n in the balanced SLJ (Arrangement I) with FG adherends under tensile load: (a) shear stress and (b) peel stress.

4. Conclusions

In this study, the adhesive time-dependent stress distribution in a SLJ with FG adherends, possessing variable through-thickness material composition profiles was analytically and numerically investigated. For this purpose, the Reddy model was applied to the two elastic FG adherends and the standard linear solid model (Zener model) was used to express the viscoelastic behavior of the adhesive layer. The numerical scheme was used to solve the equilibrium equations and find solutions for the shear and peel stress distributions in the adhesive layer over time. The numerical results on shear and peel stress distributions were compared with those of finite element solution. Very good agreements were observed between the results of both methods. The SLJ model considered in this study included balanced and unbalanced joints, bending-extensional coupling in the adherends and different material composition profiles in the FG adherends. The obtained results showed that viscoelastic behavior of the adhesive layer plays an important role in reducing the stress concentrations that occur at the left end (unbalanced joint) or both ends (balanced joint) of the overlap region. The parametric study of the joint behavior showed that the material composition profile of the FG adherends plays an important role on reducing the stress concentration in the adhesive layer. Accordingly, selecting a

stiffer material (phase) for each FG adherend reduces the stress concentration significantly. This leads to more uniform shear stress distribution in the joint. Additionally, proper set up of the adherends in a balanced joint affects the stress concentration (at any time) in a way that if the stiffer material is placed adjacent to the adhesive, the stress concentration is decreased significantly. The intensity of this effect depends on the material composition profile of the adherends and is largest at $V_{ct} \approx 25\%$. However, this effect is decreased over the time span. In addition, according to the results, stress concentrations in the joint can be reduced by an increase in the adhesive thickness or a reduction in its Young’s modulus.

Appendix A

The coefficients a_i , b_i , c_i , and d_i in Eq. (10) are given as follow:

$$a_i = \frac{D_{11}^{(i)}}{A_{11}^{(i)}D_{11}^{(i)} - (B_{11}^{(i)})^2}$$

$$d_i = \frac{A_{11}^{(i)}}{A_{11}^{(i)}D_{11}^{(i)} - (B_{11}^{(i)})^2}$$

$$b_i = \frac{-B_{11}^{(i)}}{A_{11}^{(i)}D_{11}^{(i)} - (B_{11}^{(i)})^2}$$

$$c_i = \frac{1}{\frac{5}{6}A_{55}^{(i)}} \quad i = 1, 2 \quad (A1)$$

Appendix B

To model the viscoelastic behavior of the adhesive layer, a linear viscoelastic three-parameter solid model (the Zener model) was used (see Fig. B-1).

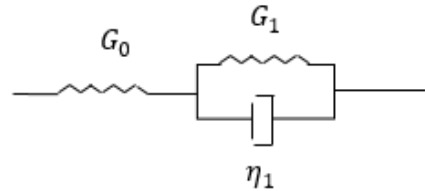


Figure B-1. Standard linear solid model (Zener model).

This model expresses the adhesive shear modulus over time in which G_0 , G_1 , and η_1 are constants used to determine the viscoelastic behavior of the adhesive layer. According to this model, G_0 is equal to G_a (the adhesive elastic shear modulus) or the adhesive shear modulus at $t = 0$. Accordingly, considering the deviatoric-volumetric component of the strain and stress tensor, the stress-strain relations for the viscoelastic adhesive layer are written as follow:

$$(P)s_{ij} = (Q)e_{ij} \quad i, j = 1, 2, 3 \quad (B1)$$

$$(\tilde{P})\tilde{s} = (\tilde{Q})\tilde{e} \quad (B2)$$

In these equations, P , Q , \tilde{P} and \tilde{Q} are the differential operators; s_{ij} and e_{ij} ($i, j = 1, 2, 3$) are the deviatoric components of the stress and strain tensor, respectively; while \tilde{s} and \tilde{e} are orderly the hydrostatic stress and strain. The differential operators in Eqs. (B1) and (B2) can be expressed as:

$$P = 1 + p_1 \frac{\partial}{\partial t} \quad , \quad Q = q_0 + q_1 \frac{\partial}{\partial t} \quad (B3)$$

$$\bar{P} = 1 \quad , \quad \bar{Q} = 3K \quad (B4)$$

Here, K is the adhesive bulk modulus in the elastic state. The changes in bulk modulus ($K=E_a G_a/3(3G_a-E_a)$) over time are assumed to be small.

Moreover, in Eq. (B3):

$$\begin{aligned} p_1 &= \frac{\eta_1}{G_0 + G_1} \\ q_0 &= \frac{G_0 G_1}{G_0 + G_1} \\ q_1 &= \frac{\eta_1 G_0}{G_0 + G_1} \end{aligned} \quad (B5)$$

The deviatoric strain and stress tensors for the plane strain condition ($\varepsilon_y = \gamma_{xy} = \gamma_{yz} = 0$), are as follow:

$$\begin{aligned} [e_{ij}] &= \begin{bmatrix} \varepsilon_x & 0 & \gamma_{xz}/2 \\ 0 & 0 & 0 \\ \gamma_{xz}/2 & 0 & \varepsilon_z \end{bmatrix} - \begin{bmatrix} \bar{\varepsilon} & 0 & 0 \\ 0 & \bar{\varepsilon} & 0 \\ 0 & 0 & \bar{\varepsilon} \end{bmatrix} \\ &= \begin{bmatrix} \varepsilon_x - \bar{\varepsilon} & 0 & \gamma_{xz}/2 \\ 0 & -\bar{\varepsilon} & 0 \\ \gamma_{xz}/2 & 0 & \varepsilon_z - \bar{\varepsilon} \end{bmatrix} \quad i, j = 1, 2, 3 \end{aligned} \quad (B6)$$

$$\begin{aligned} [s_{ij}] &= \begin{bmatrix} \sigma_x & 0 & \tau_{xz} \\ 0 & \sigma_y & 0 \\ \tau_{xz} & 0 & \sigma_z \end{bmatrix} - \begin{bmatrix} \bar{\sigma} & 0 & 0 \\ 0 & \bar{\sigma} & 0 \\ 0 & 0 & \bar{\sigma} \end{bmatrix} \\ &= \begin{bmatrix} \sigma_x - \bar{\sigma} & 0 & \tau_{xz} \\ 0 & \sigma_y - \bar{\sigma} & 0 \\ \tau_{xz} & 0 & \sigma_z - \bar{\sigma} \end{bmatrix} \quad i, j = 1, 2, 3 \end{aligned} \quad (B7)$$

Where, $\bar{\varepsilon}$ and $\bar{\sigma}$ are the hydrostatic strain and stress. For plane-strain condition one can write:

$$\bar{\varepsilon} = \frac{1}{3} (\varepsilon_x + \varepsilon_z) \quad (B8)$$

$$\bar{\sigma} = \frac{1}{3} (\sigma_x + \sigma_z + \sigma_y) \quad (B9)$$

Inserting Eqs. (B6) to (B9) into Eqs. (B1) and (B2) and eliminating σ_x and σ_y , the result will be:

$$(3P)\sigma - (3KP + 2Q)\varepsilon_z - (3KP - Q)\varepsilon_x = 0 \quad (B10)$$

$$(P)\tau = \left(\frac{1}{2}Q\right)\gamma_{xy} \quad (B11)$$

For simplicity, the shear stress τ_{xz} , and the peel stress σ_z in the adhesive are shown by τ and σ , respectively. Equation (B10) can be recast as:

$$\left(c_1 + c_2 \frac{\partial}{\partial t}\right)\sigma - \left(c_3 + c_4 \frac{\partial}{\partial t}\right)\varepsilon_z - \left(c_5 + c_6 \frac{\partial}{\partial t}\right)\varepsilon_x = 0 \quad (B12)$$

In which coefficients c_1 to c_6 are as follow:

$$\begin{aligned} c_1 &= 3 \quad , \quad c_2 = 3p_1 \\ c_3 &= 3K + 2q_0 \quad , \quad c_4 = 3Kp_1 + 2q_1 \\ c_5 &= 3K - q_0 \quad , \quad c_6 = 3Kp_1 - q_1 \end{aligned} \quad (B13)$$

Moreover, according to Eq. (B11) one can write:

$$\left(1 + p_1 \frac{\partial}{\partial t}\right)\tau = \frac{1}{2}\left(q_0 + q_1 \frac{\partial}{\partial t}\right)\gamma_{xy} \quad (B14)$$

Applying Laplace transform on both sides of Eqs. (B12) and (B14), they are converted to simple forms that are given as Eqs. (15) and (16) in section 2 of the manuscript. The coefficients introduced in these two equations are:

$$\begin{aligned} \bar{A}_1 &= \frac{(c_3 + c_4 s)}{(c_1 + c_2 s)} \\ \bar{A}_2 &= \frac{(c_5 + c_6 s)}{(c_1 + c_2 s)} \\ \bar{A}_3 &= \frac{(q_0 + q_1 s)}{2(1 + p_1 s)} \end{aligned} \quad (B15)$$

where 's' is the Laplace parameter and is called the complex variable.

Appendix C

Applying Laplace transform on both sides of Eqs. (12) and (13) and substituting the results back into Eq. (15), one can write:

$$\begin{aligned} \bar{\sigma} &= \frac{\bar{A}_1}{t_a} (\bar{w}_1 - \bar{w}_2) \\ &\quad + \frac{\bar{A}_2}{2} \left(\frac{\partial \bar{u}_1}{\partial x} - h_1 \frac{\partial \bar{\varphi}_1}{\partial x} + \frac{\partial \bar{u}_2}{\partial x} + h_2 \frac{\partial \bar{\varphi}_2}{\partial x} \right) \end{aligned} \quad (C1)$$

Furthermore, substitution of the Laplace transformed form of Eq. (10) into Eq. (C1), yields:

$$\begin{aligned} \bar{\sigma} &= \frac{\bar{A}_1}{t_a} (\bar{w}_1 - \bar{w}_2) \\ &\quad + \frac{\bar{A}_2}{2} [(a_1 - h_1 b_1) \bar{N}_1 + (a_2 + h_2 b_2) \bar{N}_2 \\ &\quad + (b_1 - h_1 d_1) \bar{M}_1 + (b_2 + h_2 d_2) \bar{M}_2] \end{aligned} \quad (C2)$$

Similarly, applying a Laplace transform on both sides of Eq. (14) and substituting the result back into Eq. (16), gives:

$$\bar{\tau} = \frac{\bar{A}_3}{t_a} (\bar{u}_1 - h_1 \bar{\varphi}_1 - \bar{u}_2 - h_2 \bar{\varphi}_2) \quad (C3)$$

On sequential differentiation of Eqs. (C2) and (C3) with respect to x , and using the Laplace transformed form of Eqs. (10) and (11), Eqs. (17) and (18) in section 2 are determined. The coefficients in Eqs. (17) and (18) are:

$$\alpha_1 = \frac{\bar{A}_2}{2} [(b_2 + h_2 d_2)(h_2 + h_a) + (a_2 + h_2 b_2) + (b_1 - h_1 d_1)(h_1 + h_a) - (a_1 - h_1 b_1)] \quad (C4)$$

$$\alpha_2 = \frac{\bar{A}_2}{2} [(b_2 + h_2 d_2) - (b_1 - h_1 d_1)] - \frac{\bar{A}_1}{t_a} (c_1 + c_2) \quad (C5)$$

$$\alpha_3 = \frac{\bar{A}_1}{t_a} [(b_1 + b_2) + d_2(h_2 + h_a) - d_1(h_1 + h_a)] \quad (C6)$$

$$\alpha_4 = \frac{\bar{A}_1}{t_a} (d_1 + d_2) \quad (C7)$$

$$\begin{aligned} \beta_1 &= \frac{\bar{A}_3}{t_a} [(b_1 - h_1 d_1)(h_1 + h_a) - (a_1 - h_1 b_1) \\ &\quad - (b_2 + h_2 d_2)(h_2 + h_a) - (a_2 + h_2 b_2)] \end{aligned} \quad (C8)$$

$$\beta_2 = -\frac{\bar{A}_3}{t_a} [(b_1 - h_1 d_1) + (b_2 + h_2 d_2)] \quad (C9)$$

Appendix D

The boundary conditions of the joint (overlap) region can be written as:

$$\int_{-l}^l \bar{\tau}(x, s) dx = \bar{N}_2|_{x=-l} - \bar{N}_2|_{x=l} \quad (D1)$$

$$\int_{-l}^l \bar{\sigma}(x, s) dx = \bar{Q}_2|_{x=-l} - \bar{Q}_2|_{x=l} \quad (D2)$$

$$\begin{aligned} \int_{-l}^l \bar{\sigma}(x, s) x dx &= (\bar{M}_2|_{x=l} - \bar{M}_2|_{x=-l}) - l (\bar{Q}_2|_{x=l} + \bar{Q}_2|_{x=-l}) \\ &\quad - (h_2 + h_a) (\bar{N}_2|_{x=l} - \bar{N}_2|_{x=-l}) \end{aligned} \quad (D3)$$

$$\frac{\partial^2 \bar{\sigma}}{\partial x^2} \Big|_{x=l} + \alpha_1 \frac{\partial \bar{\tau}}{\partial x} \Big|_{x=l} + \alpha_2 \bar{\sigma} \Big|_{x=l} = \frac{\bar{A}_1}{t_a} [(b_2 \bar{N}_2|_{x=l} + d_2 \bar{M}_2|_{x=l}) - (b_1 \bar{N}_1|_{x=l} + d_1 \bar{M}_1|_{x=l})] \quad (D4)$$

$$\frac{\partial^3 \bar{\sigma}}{\partial x^3} \Big|_{x=l} + \alpha_1 \frac{\partial^2 \bar{\tau}}{\partial x^2} \Big|_{x=l} + \alpha_2 \frac{\partial \bar{\sigma}}{\partial x} \Big|_{x=l} + \alpha_3 \bar{\tau} \Big|_{x=l} = \frac{\bar{A}_1}{t_a} (d_2 \bar{Q}_2|_{x=l} - d_1 \bar{Q}_1|_{x=l}) \quad (D5)$$

$$\frac{\partial \bar{\tau}}{\partial x} \Big|_{x=l} = \frac{\bar{A}_3}{t_a} \{ [(a_1 - h_1 b_1) \bar{N}_1|_{x=l} + (b_1 - h_1 d_1) \bar{M}_1|_{x=l}] - [(a_2 + h_2 b_2) \bar{N}_2|_{x=l} + (b_2 + h_2 d_2) \bar{M}_2|_{x=l}] \} \quad (D6)$$

$$\frac{\partial^2 \bar{\tau}}{\partial x^2} \Big|_{x=l} + \beta_1 \bar{\tau} \Big|_{x=l} = \frac{\bar{A}_3}{t_a} [(b_1 - h_1 d_1) \bar{Q}_1|_{x=l} - (b_2 + h_2 d_2) \bar{Q}_2|_{x=l}] \quad (D7)$$

Note: Eqs. (D1) to (D3) are determined based on the forces and moment equilibrium (see Fig. D-1). Moreover, owing to the fact that these equations are written in Laplace domain, with regard to Eq. (D1), since at $x=-l$, $\bar{N}_2 = \bar{N}_2^* = 0$ ($\bar{N}_2^* = 0$, free end), and at $x=l$, $\bar{N}_2 = \bar{N}_2^* = \bar{T}$ (please refer to Eq. (D10)), the expression $\bar{N}_2|_{x=-l} - \bar{N}_2|_{x=l}$ has the same physical meaning as being equal to \bar{T} in Laplace domain (or T in physical domain, as shown in Fig. 1).

Additionally, Eq. (D2) is based on the equilibrium of forces stemming from the boundary conditions (please note that at $x = -l$, $\bar{Q}_2|_{x=-l} = 0$ (or $Q_2|_{x=-l} = 0$, outside the Laplace domain). However, to write Eq. (D3), the proposed model postulated in Ref. [43] was used (also used by many others). This model was deduced based on the fact that for the joint to be in shear, the moment created by the applied forces at the two ends of the assembly must be equal to zero. As a result, the applied forces at the two extreme ends are assumed to be collinear, forming an angle $\alpha = (t_1 + t_2 + 2t_a)/2(L_1 + L_2 + 2l)$ with respect to the horizontal direction. This produces a total moment of zero on the whole structure. Such applied forces produce horizontal and vertical components T and αT , at each end (see Fig. 5). Doing so, the two vertical forces created at the two extreme ends of the structure create a moment that counterbalance the moment due to tensile force T . Obviously, these forces will be present in the corresponding free body diagrams (see Figs. D-1 and D-2) used to derive the governing equations.

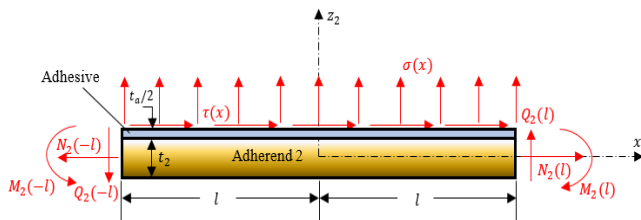


Figure D-1. The free-body diagram of the adherend 2 in the overlap region.

According to the boundary conditions at the two ends of the overlap region (see Fig. D-2), one can write:

References

[1] M. Banea, L. F. da Silva, Adhesively bonded joints in composite materials: an overview, *Proceedings of the Institution of Mechanical Engineers, Part L: Journal of Materials: Design and Applications*, Vol. 223, No. 1, pp. 1-18, 2009.

$$\text{@ } x = -l : \bar{N}_1 = \bar{N}_1^* , \bar{M}_1 = -\bar{M}_1^* , \bar{Q}_1 = \bar{Q}_1^* \quad (D8)$$

$$\bar{N}_2 = \bar{M}_2 = \bar{Q}_2 = 0$$

$$\text{@ } x = l : \bar{N}_1 = \bar{M}_1 = \bar{Q}_1 = 0 \quad (D9)$$

$$\bar{N}_2 = \bar{N}_2^* , \bar{M}_2 = \bar{M}_2^* , \bar{Q}_2 = \bar{Q}_2^*$$

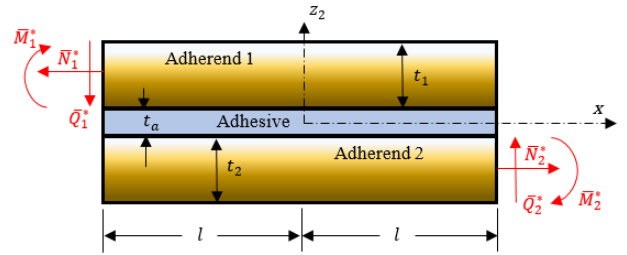


Figure D-2. The boundary conditions at two ends of joint region.

Equations (D8) and (D9) are written based on the boundary conditions. They can be easily extracted by a glance at the geometry of the joint (Fig. 1) or Fig. D-2. where, N_1^* , Q_1^* , M_1^* and N_2^* , Q_2^* , M_2^* are the boundary loads at the two ends of the overlap region. According to Fig. D-2, as well as the loading condition given for the SLJ, one can write [43]:

$$\bar{N}_1^* = \bar{T} , \bar{N}_2^* = \bar{T} \quad (D10)$$

$$\bar{Q}_1^* = \bar{Q}_2^* = \frac{(1 - k_1^* - k_2^*)(h_1 + h_2)\bar{T}}{2l}$$

$$\bar{M}_1^* = k_1^*(h_1 + h_2)\bar{T} , \bar{M}_2^* = k_2^*(h_1 + h_2)\bar{T}$$

Here, k_1^* and k_2^* are the edge moments correction factors for the SLJ and are defined as [43]:

$$k_1^* = \xi_2 / (\xi_1 + 2\xi_1\xi_2l + \xi_2) \quad (D11)$$

$$k_2^* = \xi_1 / (\xi_1 + 2\xi_1\xi_2l + \xi_2)$$

where:

$$\xi_1 = \sqrt{d_1 \bar{T}} , \xi_2 = \sqrt{d_2 \bar{T}} , \bar{T} = \frac{T}{s} \quad (D12)$$

It is worth to mention that Eq. (D12) has been extracted from Ref. [43]. Please refer to Eqs. (18) and (19) in this Reference for more details.

It is assumed that the tensile load is constant and the transient effects of the initial loading are ignored. On proper substitution of Eqs. (21) and (22) in the boundary conditions (Eqs. (D1) to (D7)), a set of equations are obtained. Solving these equations, the unknown coefficients in Eqs. (21) and (22) can be determined.

Appendix E

The coefficients in Eqs. (25) and (26) are as follow:

$$\alpha_2 = - \left(\bar{A}_2(b_1 - h_1 d_1) + \frac{\bar{A}_1}{h_a}(c_1) \right) , \alpha_4 = \frac{\bar{A}_1}{h_a}(d_1) \quad (E1)$$

$$\beta_1 = \frac{\bar{A}_3}{h_a} [(b_1 - h_1 d_1)(h_1 + h_a) - (a_1 - h_1 b_1)] \quad (E2)$$

[2] L. F. da Silva, P. J. das Neves, R. Adams, J. Spelt, Analytical models of adhesively bonded joints— Part I: Literature survey, *International Journal of Adhesion and Adhesives*, Vol. 29, No. 3, pp. 319-330, 2009.

[3] L. F. da Silva, P. J. das Neves, R. Adams, A. Wang, J. Spelt, Analytical models of adhesively bonded

- joints—Part II: Comparative study, *International Journal of Adhesion and Adhesives*, Vol. 29, No. 3, pp. 331-341, 2009.
- [4] X. He, A review of finite element analysis of adhesively bonded joints, *International Journal of Adhesion and Adhesives*, Vol. 31, No. 4, pp. 248-264, 2011.
- [5] S. Budhe, M. Banea, S. De Barros, L. Da Silva, An updated review of adhesively bonded joints in composite materials, *International Journal of Adhesion and Adhesives*, Vol. 72, pp. 30-42, 2017.
- [6] M. Shishesaz, M. Hosseini, Effects of joint geometry and material on stress distribution, strength and failure of bonded composite joints: an overview, *The Journal of Adhesion*, pp. 1-69, 2018.
- [7] O. Volkersen, Stress distribution of bonded joint under tensile stress with constant cross section of straps, *Aerospace research*, Vol. 15, pp. 41-68, 1938.
- [8] M. Goland, The stresses in cemented joints, *J. appl. Mech.*, Vol. 17, pp. 66, 1944.
- [9] L. J. Hart-Smith, Adhesive bonded Double-lap joints, *NASA Langley Contract Report*, 1973.
- [10] Q. Luo, L. Tong, Analytical solutions for adhesive composite joints considering large deflection and transverse shear deformation in adherends, *International Journal of Solids and Structures*, Vol. 45, No. 22-23, pp. 5914-5935, 2008.
- [11] Q. Luo, L. Tong, Linear and higher order displacement theories for adhesively bonded lap joints, *International journal of solids and structures*, Vol. 41, No. 22-23, pp. 6351-6381, 2004.
- [12] Q. Luo, L. Tong, Analytical solutions for nonlinear analysis of composite single-lap adhesive joints, *International Journal of Adhesion and Adhesives*, Vol. 29, No. 2, pp. 144-154, 2009.
- [13] B. Zhao, Z.-H. Lu, Y.-N. Lu, Closed-form solutions for elastic stress-strain analysis in unbalanced adhesive single-lap joints considering adherend deformations and bond thickness, *International Journal of Adhesion and Adhesives*, Vol. 31, No. 6, pp. 434-445, 2011.
- [14] E. Selahi, M. Tahani, S. A. Yousefsani, Analytical solutions of stress field in adhesively bonded composite single-lap joints under mechanical loadings, *Int J Eng*, Vol. 27, No. 3, pp. 475-486, 2014.
- [15] Z. Liu, Y. Huang, Z. Yin, S. Bennati, P. S. Valvo, A general solution for the two-dimensional stress analysis of balanced and unbalanced adhesively bonded joints, *International Journal of Adhesion and Adhesives*, Vol. 54, pp. 112-123, 2014.
- [16] B. Zhao, Z.-H. Lu, Y.-N. Lu, Two-dimensional analytical solution of elastic stresses for balanced single-lap joints—Variational method, *International Journal of Adhesion and Adhesives*, Vol. 49, pp. 115-126, 2014.
- [17] M. Shishesaz, A. Reza, M. Daniali, Stress distribution in single lap joints with a cracked composite adherend—part I: single lamina adherends, *The Journal of Adhesion*, Vol. 90, No. 11, pp. 912-931, 2014.
- [18] M. Shishesaz, A. Reza, M. Daniali, Stress distribution in single lap joints with a cracked composite adherend—part II: laminated adherends, *The Journal of Adhesion*, Vol. 90, No. 12, pp. 933-954, 2014.
- [19] Z. Jiang, S. Wan, Z. Zhong, M. Li, Geometrically nonlinear analysis for unbalanced adhesively bonded single-lap joint based on flexible interface theory, *Archive of Applied Mechanics*, Vol. 86, No. 7, pp. 1273-1294, 2016.
- [20] Z. Jiang, S. Wan, T. Keller, A. P. Vassilopoulos, Two-dimensional analytical stress distribution model for unbalanced FRP composite single-lap joints, *European Journal of Mechanics-A/Solids*, Vol. 66, pp. 341-355, 2017.
- [21] E. Selahi, M. Kadivar, Non-linear Analysis of Adhesive Joints in Composite Structures, *Composite Structures*, Vol. 9, No. 1, pp. 83-92, 2016.
- [22] A. T. l'Armée, N. Stein, W. Becker, Bending moment calculation for single lap joints with composite laminate adherends including bending-extensional coupling, *International Journal of Adhesion and Adhesives*, Vol. 66, pp. 41-52, 2016.
- [23] F. Delale, F. Erdogan, Viscoelastic analysis of adhesively bonded joints, *Journal of Applied Mechanics*, Vol. 48, No. 2, pp. 331-338, 1981.
- [24] P. Pandey, H. Shankaragouda, A. K. Singh, Nonlinear analysis of adhesively bonded lap joints considering viscoplasticity in adhesives, *Computers & structures*, Vol. 70, No. 4, pp. 387-413, 1999.
- [25] Y. Nagaraja, R. Alwar, Viscoelastic analysis of an adhesive-bonded plane lap joint, *Computers & Structures*, Vol. 11, No. 6, pp. 621-627, 1980.
- [26] S. Yadagiri, C. P. Reddy, T. S. Reddy, Viscoelastic analysis of adhesively bonded joints, *Computers & structures*, Vol. 27, No. 4, pp. 445-454, 1987.
- [27] W. C. Carpenter, Viscoelastic analysis of bonded connections, *Computers & Structures*, Vol. 36, No. 6, pp. 1141-1152, 1990.
- [28] H. L. Groth, Viscoelastic and viscoplastic stress analysis of adhesive joints, *International Journal of Adhesion and Adhesives*, Vol. 10, No. 3, pp. 207-213, 1990.
- [29] C. Sato, Stress estimation of joints having adherends with different curvatures bonded with viscoelastic adhesives, *International Journal of Adhesion and Adhesives*, Vol. 31, No. 5, pp. 315-321, 2011.
- [30] M. Shishesaz, A. Reza, The effect of viscoelasticity of polymeric adhesives on shear stress distribution in a single-lap joint, *The Journal of Adhesion*, Vol. 89, No. 11, pp. 859-880, 2013.
- [31] A. Reza, M. Shishesaz, The effect of viscoelasticity on the stress distribution of adhesively single-lap joint with an internal break in the composite adherends, *Mechanics of Time-Dependent Materials*, Vol. 22, No. 3, pp. 373-399, 2018.
- [32] A. Reza, M. Shishesaz, K. Naderan-Tahan, The effect of viscoelasticity on creep behavior of double-lap adhesively bonded joints, *Latin American Journal of Solids and Structures*, Vol. 11, No. 1, pp. 35-50, 2014.

- [33] A. Reza, M. Shishesaz, Transient load concentration factor due to a sudden break of fibers in the viscoelastic PMC under tensile loading, *International Journal of Solids and Structures*, Vol. 88, pp. 1-10, 2016.
- [34] N. Stein, P. Weißgraeber, W. Becker, Stress solution for functionally graded adhesive joints, *International Journal of Solids and Structures*, Vol. 97, pp. 300-311, 2016.
- [35] N. Stein, H. Mardani, W. Becker, An efficient analysis model for functionally graded adhesive single lap joints, *International Journal of Adhesion and Adhesives*, Vol. 70, pp. 117-125, 2016.
- [36] N. Stein, J. Felger, W. Becker, Analytical models for functionally graded adhesive single lap joints: A comparative study, *International journal of adhesion and adhesives*, Vol. 76, pp. 70-82, 2017.
- [37] N. Stein, P. Rosendahl, W. Becker, Homogenization of mechanical and thermal stresses in functionally graded adhesive joints, *Composites Part B: Engineering*, Vol. 111, pp. 279-293, 2017.
- [38] M. K. Apalak, R. Gunes, Investigation of elastic stresses in an adhesively bonded single lap joint with functionally graded adherends in tension, *Composite structures*, Vol. 70, No. 4, pp. 444-467, 2005.
- [39] M. K. Apalak, R. Gunes, Elastic flexural behaviour of an adhesively bonded single lap joint with functionally graded adherends, *Materials & design*, Vol. 28, No. 5, pp. 1597-1617, 2007.
- [40] W. E. Guin, J. Wang, Theoretical model of adhesively bonded single lap joints with functionally graded adherends, *Engineering Structures*, Vol. 124, pp. 316-332, 2016.
- [41] S. Amidi, J. Wang, Three-parameter viscoelastic foundation model of adhesively bonded single-lap joints with functionally graded adherends, *Engineering Structures*, Vol. 170, pp. 118-134, 2018.
- [42] M. Khan, S. Kumar, J. Reddy, Material-tailored adhesively bonded multilayers: A theoretical analysis, *International Journal of Mechanical Sciences*, Vol. 148, pp. 246-262, 2018.
- [43] X. Zhao, R. Adams, L. F. da Silva, A new method for the determination of bending moments in single lap joints, *International Journal of Adhesion and Adhesives*, Vol. 30, No. 2, pp. 63-71, 2010.